Applied Surface Science 580 (2022) 152319

Contents lists available at ScienceDirect

Applied Surface Science

journal homepage: www.elsevier.com/locate/apsusc

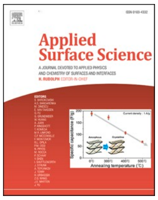

Full Length Article

Green self-derived templating preparation of nitrogen, sulfur co-doped porous carbon/tin composites with synergistic effect towards high-performance lithium-ion batteries

Kun Liu [a,1], Hongfei Zheng [b,1], Jia-ao Wang [c,1], Yuhao Zhou [a], Ning Zhang [a], Yehong Du [a], Jianzong Man [a], Graeme Henkelman [c], Juncai Sun [a,*]

[a] *Institute of Materials and Technology, Dalian Maritime University, Dalian 116026, China*
[b] *College of Materials, Xiamen University, Xiamen 361005, China*
[c] *Department of Chemistry and the Oden Institute for Computational Engineering and Sciences, The University of Texas at Austin, Austin, TX 78712-0165, USA*

ARTICLE INFO

Keywords:
Self-derived templating
Nitrogen, sulfur co-doped porous carbon
Sn particles
Synergistic effect
Lithium-ion batteries

ABSTRACT

Although single-heteroatom doped porous carbon/tin (Sn) composites have been extensively studied, an overall understanding of the effects of dual-heteroatoms doped porous carbon on the lithium storage properties of Sn is still insufficient. Herein, we provide a green self-derived templating strategy to synthesize the nitrogen, sulfur co-doped porous carbon/Sn composites (Sn/NSPC) with synergistic effect through one-step carbonization. The key to this approach is the self-generation of Na_2CO_3 template, and it is apt to eliminate with water directly. The resultant NSPC can prevent the agglomeration of Sn particles. The synergistic effect is confirmed by density functional theoretical (DFT) calculations, revealing that N, S co-doped improves the electronic conductivity. The lithium storage mechanism and structural stability of Sn/NSPC electrode are researched via in-situ XRD and ex-situ XPS. The obtained electrode affords a discharge capacity (200 cycles, 712.6 mAh/g at 0.1 A/g) and long-life cyclability (2000 cycles, 330.1 mAh/g at 3 A/g). Additionally, the Sn/NSPC||$LiCoO_2$ full cell achieves excellent discharge capacity (572.6 mAh/g at 0.1 A/g) while remaining impressive cyclability (440.6 mAh/g at 1 A/g). This green and eco-friendly approach may be extended to the preparation of other heteroatom-doped carbon/Sn composites.

1. Introduction

On account of the ever-growing requirements of power sources for hand-held electronic apparatus and EVs, lithium-ion batteries (LIBs) possessing high energy density have captured tremendous interest [1–3]. Since the graphite anode possesses relatively poor specific capacity (372 mAh/g) [4]. great efforts have been attempted on the development and preparation of alternative anode materials. Of the alternative candidates designed, tin (Sn) exhibits tremendous potential thanks to its large specific capacity (993 mAh/g) and proper operation voltage [5,6]. Nonetheless, the massive volume variation of Sn upon cycling results in inferior cycling life [7,8].

Considerable strategies have been taken to tackle the foregoing obstacles, including preparing nanostructures [9] ,constructing a thin film [10] or incorporating Sn with inactive metal elements [11,12], metal oxide [13] and carbon matrices [8,14,15]. Among these, the introduction of carbon matrices is regarded as to be one of the most efficacious strategies to heighten the electrochemical properties of the Sn anode [16]. Particularly porous carbon (PC) is exceptionally appealing as matrix materials because it could provide short pathway for ion transportation and raise the electrode contact with electrolyte [17]. When coupled with Sn anode, the porous structure provides extra buffer space for volume change of Sn and reduces the pulverization of Sn. Consequently, the electrochemical properties of the Sn anode can be greatly heightened.

Recently, heteroatom doping has been recognized as a valid way to tailor and ameliorate the physical and chemical properties of PC materials [18,19]. Among various heteroatoms, the incorporation of nitrogen (N) could introduce defects in carbon matrix, fortify the electronic conductivity and supply more active sites, which is helpful for Li^+

---

* Corresponding author.
E-mail address: sunjc@dlmu.edu.cn (J. Sun).

[1] These authors contributed equally to this work.

https://doi.org/10.1016/j.apsusc.2021.152319
Received 24 October 2021; Received in revised form 21 December 2021; Accepted 22 December 2021

storage [20,21]. The incorporation of sulfur (S) can alter the charge state of the neighboring C atoms, enhancing adsorption ability [22]. Furthermore, S possesses larger atomic radius and smaller electronegativity, contributing to promoting Li^+ diffusion [23]. It could supply extra electron transfer path via C-S-C bond as well [23]. Meanwhile, S doping is of great importance to increase the electrochemical activity of electrode materials [24]. Given the individual characteristics of single element doping for the enhancement of solely one aspect of properties, it would be interesting to develop the PC materials with multi-element doping, which is hopeful for ameliorating the overall performance of the materials in view of the synergetic effect from the heteroatoms. Typically, heteroatom doping PC materials could be achieved by templating method, where the porous structure is formed via in situ doping heteroatom-embodying organics on the surface of templates, and then through organic calcination and template removal [17]. However, templating methods previously reported generally need the tedious multiple steps, high-cost raw materials and harmful chemical reagents, enabling it hard to mass production and unsuitable for practical application. As a consequence, it will be greatly interesting to design a simple, cost-effective and environmentally friendly self-derived templating strategy for preparing dual-heteroatoms doped PC materials. More importantly, the N, S co-doped PC has been widely researched in the fields of Li-S batteries, supercapacitors, and LIBs [25–27], but has not been employed in the Sn anode of LIBs so far.

In this work, we use low-cost thiourea (CH_4N_2S) and disodium stannous citrate (DSSC) as raw materials to construct N, S co-doped porous C/Sn composites (Sn/NSPC) via a facile self-derived templating method, followed by removal of self-derived Na_2CO_3 template with water directly, which avoids the tedious synthesis processes, expensive raw materials and toxic chemical solvents in most template preparations. The pores are formed by the release of gas during the carbonization process. And the self-derived template (Na_2CO_3) can further boost the formation of pores. The formed pore structure can supply sufficient diffusion channels for ion transportation and alleviate volume change upon cycling. Furthermore, NSPC could arrest the agglomeration of Sn particles. Meanwhile, NSPC could produce more active sites and defects, improve the reactivity, conductivity, and increase the lithium storage capacity of the anode materials. The synergistic effect is demonstrated by Density Functional Theoretical (DFT) calculations, suggesting that the NSPC could significantly raise the electronic conductivity, which is instrumental in promoting the electron transfer and enhancing the lithium storage capacity. Accordingly, Sn/NSPC electrode achieves high discharge capacity, outstanding rate capability and long-life cyclability. A full cell Sn/NSPC||$LiCoO_2$ is also assembled and provides a high discharge capacity.

2. Experimental section

2.1. Preparation of samples

The Sn/NSPC composite was synthesized via a simple one-step carbonization process in a tube furnace, as displayed in Scheme 1. Typically, 4 g of DSSC powder was mixed with 0.08 g of CH_4N_2S in a ball-milling machine, and placed in a tube furnace and heated at 750 °C for 1 h. Later the resultant powder was washed by deionized water to eliminate the self-derived template (Na_2CO_3) and finally obtained Sn/NSPC composite. As comparison, the Sn/PC was made via the same process except for the absence of CH_4N_2S. The nitrogen-doped porous carbon/Sn composite (Sn/NPC) was also made under the same conditions in the existence of urea.

2.2. Characterization

Scanning electron microscope (SEM, SUPER55/SAPPHIRE) and transmission electron microscopy (TEM, FEI Talos F200S) were utilized to record the morphology of samples. The Brunauer–Emmett–Teller (BET) surface area was assessed by N_2 adsorption/desorption isotherms measurement. X-ray diffraction (XRD, Rigaku-D/MAX-3A with Co-Kα radiation) was utilized to identify the crystal structure of products. Raman spectra were performed by Raman system. Thermogravimetric analysis (TGA) was implemented with a NETZSCH-STA409C instrument. X-ray photoelectron spectroscopy (XPS) was conducted to analyze the composition of samples. The in-situ XRD data were acquired via a Rikagu Ultima IV instrument at 150 mA/g.

2.3. Electrochemical measurements

Acetylene black (20 wt%), carboxymethyl cellulose (10 wt%) and active substance (70 wt%) were grinded in deionized water to form homogeneous slurry, which was then coated on Cu foil. The loading mass and thickness of the electrode were approximately 1.0–1.2 mg/cm^2 and 20 μm, respectively. The coin-type cells (CR2032) were installed in a glove box with Li foil (as counter electrode and reference electrode) and Celgard 2400 (as separator). 1 M $LiPF_6$ in a mixture of ethylene carbonate/dimethyl carbonate (1:1, v/v) was utilized as electrolyte. Galvanostatic charge/discharge (GCD) and galvanostatic intermittent

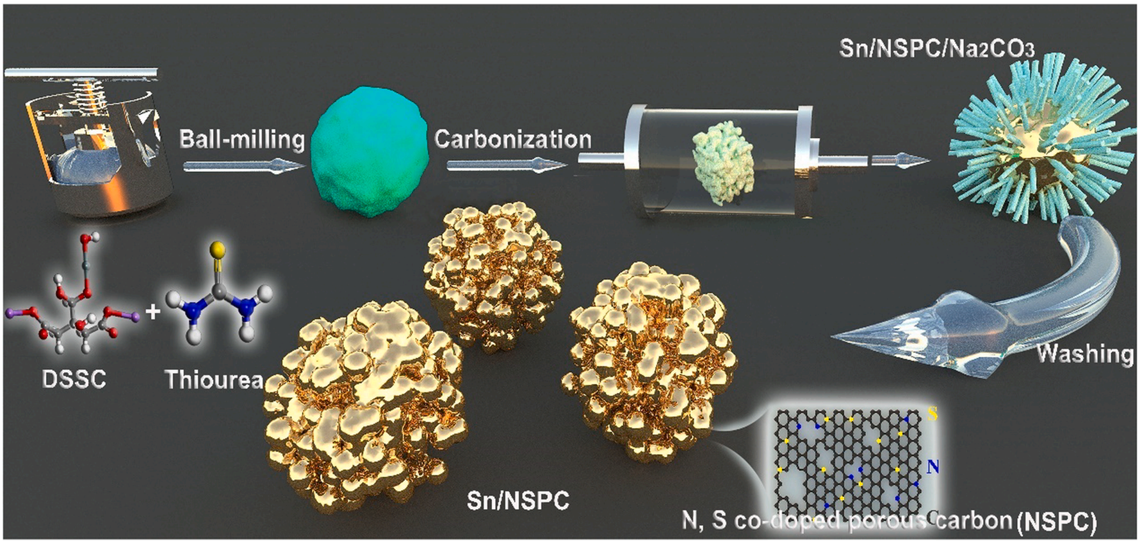

Scheme 1. Schematic diagram of the fabrication processes of Sn/NSPC composite.

titration technique (GITT) measurements were conducted from 0.01 to 3.0 V applying LAND-CT2001A. Cyclic voltammetry (CV) profiles and electrochemical impedance spectra (EIS) data were obtained employing a CHI660D electrochemical workstation. The full cells are assembled using prelithiated Sn/NSPC as anode and $LiCoO_2$ as cathode. The fabrication process of $LiCoO_2$ electrode was the same as that of Sn/NSPC except that the Cu foil was changed to Al foil. The active weight ratio between cathode and anode was around 5.5:1. To ameliorate the coulombic efficiency, the Sn/NSPC anode was prepared by the pre-lithiation process. The Sn/NSPC||$LiCoO_2$ full cells are cycled within 1.0–3.8 V. The specific capacity of the full cell was obtained from the weight of Sn/NSPC.

2.4. Computational methods

The detailed computational methods [28-30] are available in Supporting information.

3. Results and discussion

The morphology and microstructure of hybrids were harvested by SEM and TEM. Fig. S1 describes the morphology of unwashed sample after carbonization, showing the presence of self-generated template (Na_2CO_3), which is further demonstrated in XRD pattern (Fig. S2). After being rinsed with deionized water, the Na_2CO_3 template is eliminated and then PC is acquired. As portrayed in (Fig. 1a, b and c), Sn/PC, Sn/NPC and Sn/NSPC display typical morphologies of PC and Sn particles composites. Sn particles are dispersed into PC matrix, which could validly tolerate the volume change and aggregation of the Sn particles. The EDS mapping analysis unveils the distribution of Sn, C, N, S, and O elements (Fig. 1d), suggesting the co-doping of N and S into PC, which is also certified by XPS. From the TEM images (Fig. 1e and f), the Sn/NSPC depicts the distributed Sn particles with diameter of about 200–600 nm into the PC, which well supports the above SEM result. HRTEM image (Fig. 1g) reveals a lattice spacing of 0.294 nm, assigning to the (200) facet of Sn. Additionally, the TEM mapping further illustrates the distribution of Sn, C, N, S, and O elements (Fig. 1h).

The specific surface area (SSA) of Sn/PC, Sn/NPC, and Sn/NSPC products were examined via N_2 adsorption/desorption tests, as described in (Fig. 2a and b). The SSAs of the Sn/NSPC and Sn/NPC are successively 178 m^2/g and 171 m^2/g, which exceeds that of Sn/PC (141 m^2/g). Moreover, the isotherms for the three samples exhibit the typical IV curves, manifesting the presence of mesoporous structure. Compared with the Sn/NSPC, the SSA of unwashed Sn/NSPC/Na_2CO_3 is only 0.98 m^2/g, and the pore volume is negligible (Fig. S3), suggesting that the self-derived template (Na_2CO_3) hinders the generation of pores. After being rinsed with deionized water, the SSA and pore volume of the Sn/NSPC are greatly increased, which indicates the formation of pores. Therefore, the Na_2CO_3 generated by carbonization is served as a sacrificial template to support the formation of pores. The pore size distribution curves (Fig. 2b) display that mesoporous are primarily distributed at the diameter of about 3.8 nm. Higher SSA and mesoporous structure of the Sn/NSPC not only can relieve volume changes during cycling, but offer ample active sites for Li^+ diffusion and the penetration of electrolyte [31,32].

XRD patterns (Fig. 2c) exhibit that all diffraction peaks correspond to the tetragonal Sn. No peaks of C are detected, reflecting its amorphous nature [33,34]. This is also supported via the Raman spectra (Fig. 2d).

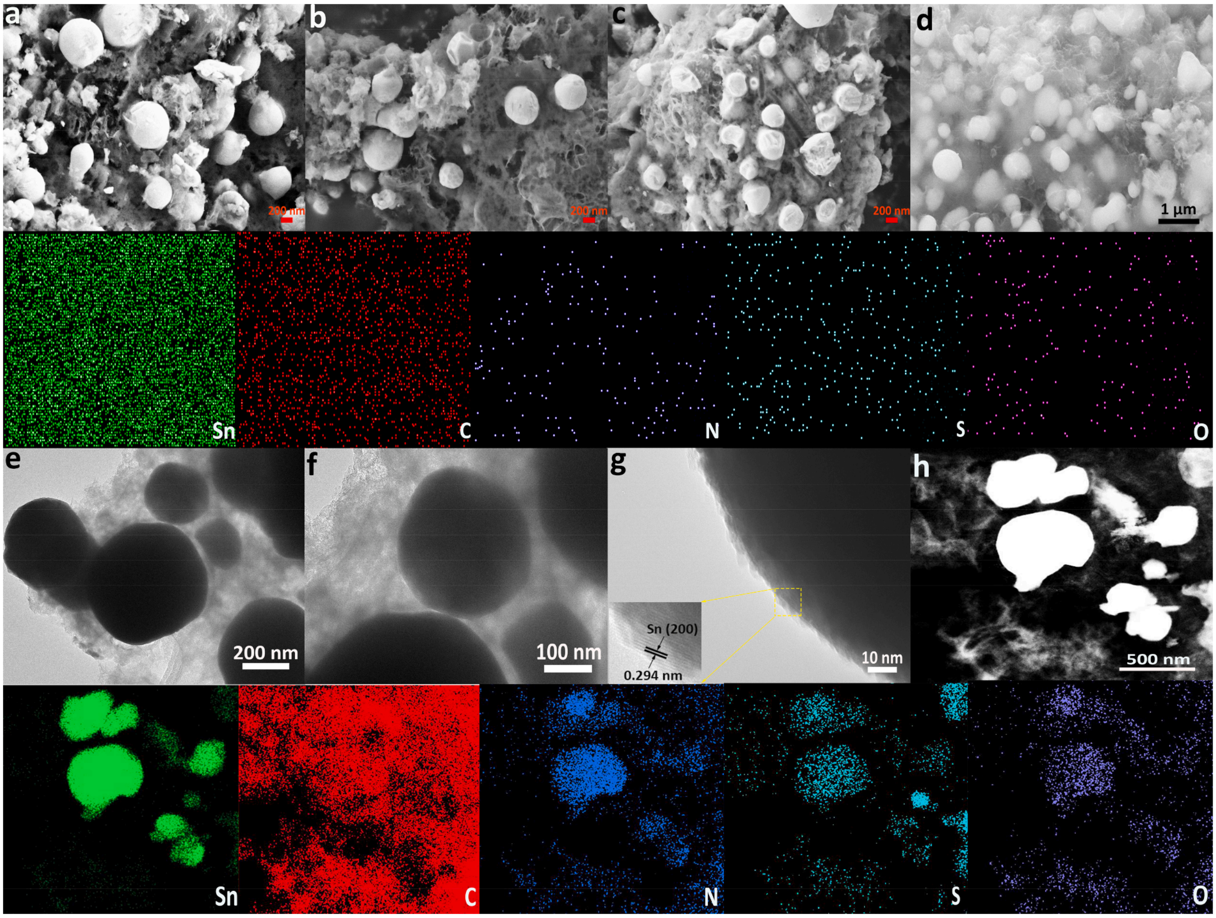

Fig. 1. SEM images of (a) Sn/PC, (b) Sn/NPC and (c) Sn/NSPC. (d) EDS mapping of Sn/NSPC. (e-f) TEM, (g) HR-TEM and (h) the corresponding mapping images of Sn/NSPC.

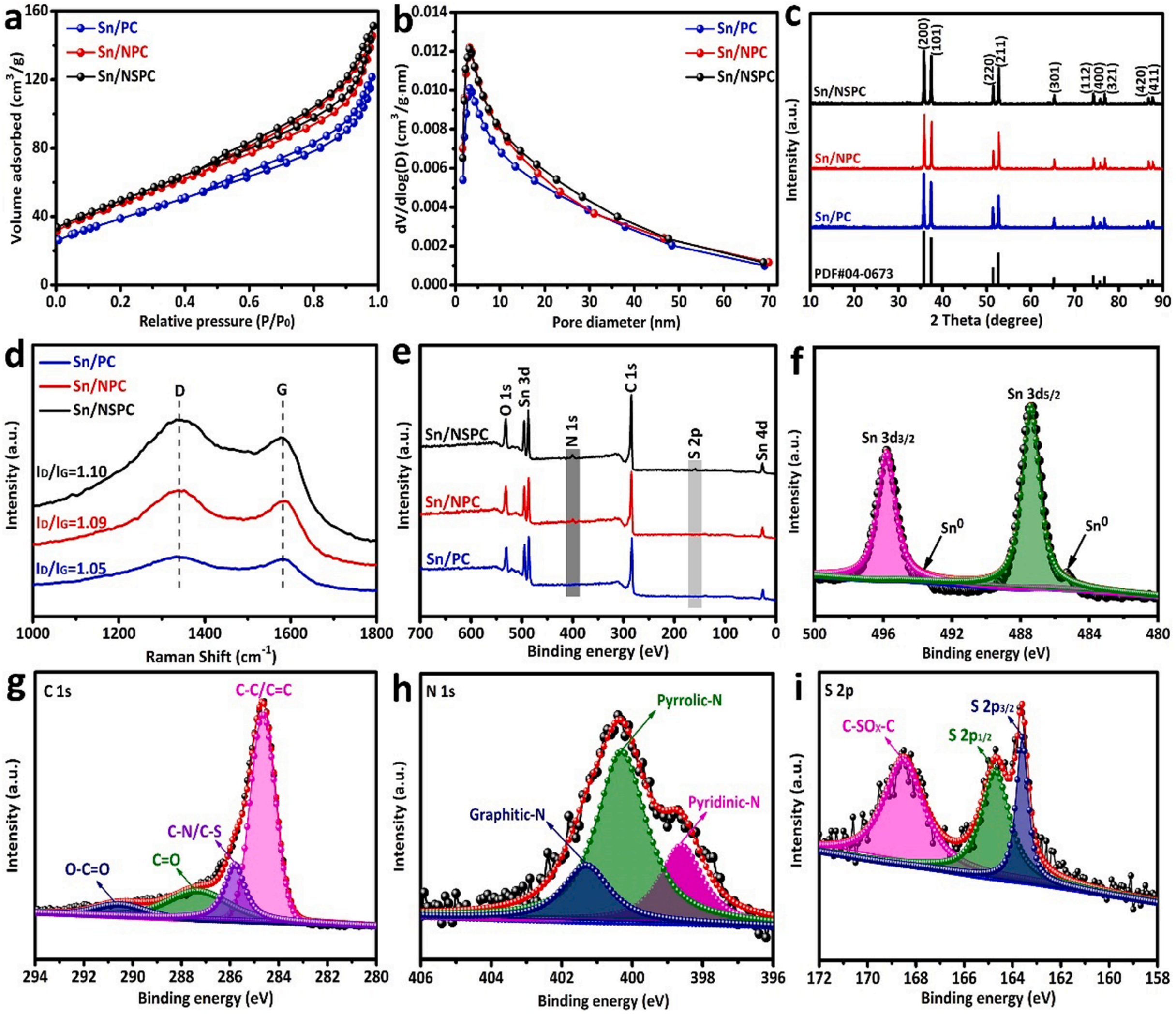

Fig. 2. (a) N_2 adsorption/desorption plots, (b) pore size distribution, (c) XRD patterns, (d) Raman spectra and (e) XPS full spectra of Sn/PC, Sn/NPC and Sn/NSPC, high-resolution of (f) Sn 3d, (g) C 1 s, (h) N 1 s and (i) S 2p spectra for Sn/NSPC.

Two peaks at approximately 1341 and 1584 cm^{-1} are indexed to the D and G bands of amorphous C [35,36]. Furthermore, the I_D/I_G of Sn/NSPC is 1.10, evidently higher than that of Sn/PC (1.05), implying that more defects are generated in the PC as a result of N, S co-doping [37,38].

To identify the surface chemical composition of samples, XPS measurement was adopted. The XPS full spectra of unwashed Sn/NSPC/Na_2CO_3 composite shows the presence of Sn, C, O, S, N and Na elements (Fig. S4), in which the Na element originates from the self-derived template (Na_2CO_3). After being rinsed with deionized water, the Na_2CO_3 template is eliminated. Therefore, the XPS full spectra of three specimens authenticate the presence of Sn, C, and O elements, but no Na element (Fig. 2e). Meanwhile, two weak peaks of N and S elements are seen in Sn/NSPC. The S and N doping contents for Sn/NPC and Sn/NSPC samples were determined by elemental analyzer (EA). The results indicate that Sn/NPC sample provides 0.71 % N, while the S and N contents of Sn/NSPC sample are 0.94% and 0.56%, respectively. The Sn 3d spectrum is deconvoluted as four peaks (Fig. 2f), two strong peaks correspond to Sn $3d_{3/2}$ (495.8 eV) and Sn $3d_{5/2}$ (487.4 eV) because of the partial surface oxidation of Sn/NSPC exposed to air [39,40]. Two weak peaks at 485.4 and 493.7 eV are derived from Sn^0. The C 1 s spectrum (Fig. 2g) is deconvoluted as four peaks at 284.7, 285.8, 287.4, and 290.6 eV, which is related to C-C/C = C, C-N/C-S, C = O, and O = C-O bonds in turn, indicating the incorporation of N and S into C matrix [23,41]. (Fig. 2h) shows that the three deconvoluted peaks originate from pyridinic-N (398.6 eV), pyrrolic-N (400.3 eV) and graphitic-N (401.3 eV), respectively [42,43]. It is well known that the pyrrolic-N and pyridinic-N can generate more defects and active sites in C matrix, contributing to facilitating the Li^+ diffusion [36,44]. The graphitic-N can heighten the electronic conductivity of C matrix [23,38]. The peaks at 163.6 and 164.7 eV (Fig. 2i) are successively identified as S $2p_{3/2}$ and S $2p_{1/2}$ of carbon-bonded thiophene-like sulfur C-S-C, and the peak at 168.5 eV is derived from C-SO_x-C [45,46]. The introduction of S could offer extra electron transfer route by C-S-C bond and meanwhile enhance the electrochemical activity of electrode materials [23]. Furthermore, thiophene-S group is helpful for increasing the reversible capacity [38]. Above analysis further demonstrates the successful co-doping of N and S into PC, beneficial for improving the electronic conductivity and reactivity, introducing active sites, and thus enhancing Li storage ability.

To investigate the lithium storage property of Sn/NSPC electrode, the initial three CV curves are given in (Fig. 3a). An irreversible reduction peak at approximately 0.6 V is seen for the first cathodic scan but disappears in the following cycles, which implies the generation of SEI film [47]. Peaks between 0.35 and 0.65 V represent the formation of Li_xSn in the cathodic scan [7,34]. In the anodic scan, the four peaks within 0.5–0.82 V are originated from the de-alloying reaction of Li_xSn [39]. In addition, there is a peak at around 3 V in the first cycle, which

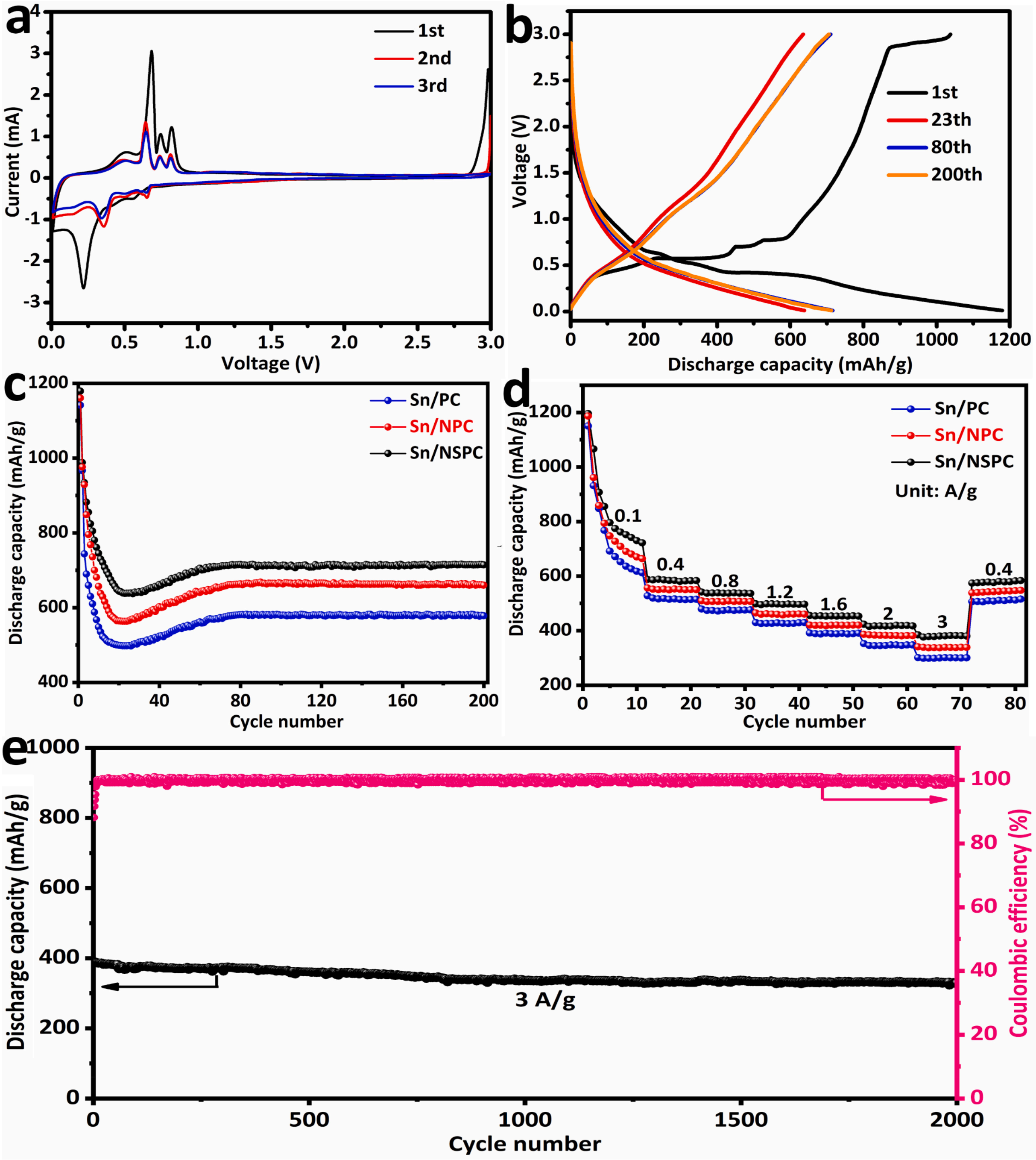

Fig. 3. (a) CV curves of Sn/NSPC at 0.2 mV/s. (b) GCD plots of Sn/NSPC. (c) Cycling performance at 0.1 A/g and (d) rate capability of Sn/PC, Sn/NPC and Sn/NSPC electrodes. (e) Cycling performance of Sn/NSPC at 3 A/g.

vanishes in the next cycles. This may be associated with the presence of oxygen in the system [48–50].

The first charge/discharge (CD) capacities of the Sn/NSPC electrode are 1037.6 and 1179.5 mAh/g in sequence (Fig. 3b), corresponding to an initial columbic efficiency (ICE) of 88.0%. The cycling performance of three electrodes is plotted in (Fig. 3c). Intriguingly, the discharge capacity of the Sn/NSPC electrode decays from 1179.5 to 638.4 mAh/g during the first 23 cycles, and then progressively raises to a maximum value of 715.8 mAh/g at the 80th cycle. After that, the capacity trends to stabilize (712.6 mAh/g) in the subsequent cycles, indicating outstanding cycling stability. The Sn/PC and Sn/NPC electrodes also undergo a similar electrochemical process. This phenomenon can be observed in many previous Sn-based anodes, which is largely related to the reversible formation of the polymeric gel-like layer deriving from electrolyte decomposition [39,44,51–53]. Compared to the Sn/NSPC electrode, the other two electrodes deliver relatively inferior discharge capacities of 578.5 and 660.3 mAh/g in several, which is because of the synergistic effect of N, S co-doping, improving the electronic conductivity, enhancing the electrochemical activity, and producing more active sites, and thus leading to more available Li^+ storage sites [38,54]. The Sn/NSPC electrode presents good electrochemical properties compared to previously Sn-based electrode materials (Table S1).

The Sn/NSPC electrode also achieves impressive high-rate capability, as unveiled in (Fig. 3d). Remarkably, the Sn/NSPC yields a discharge capacity of 384.9 mAh/g at 3 A/g, while the other two electrodes only afford 301.6 and 340.9 mAh/g. As plotted in Fig. S5, the semicircle diameter for the Sn/NSPC is smaller than that of the other two electrodes, meaning that the Sn/NSPC electrode owns lower charge-transfer impedance, which verifies that the Sn/NSPC displays higher electric conductivity owing to N, S co-doping. The long-life cycling performance of the Sn/NSPC electrode at 3 A/g was further assessed (Fig. 3e). The discharge capacity of Sn/NSPC electrode can remain at 330.1 mAh/g after 2000 cycles and the CE is close to 100%, signifying the superior cyclability.

To further evaluate the reaction kinetics of electrodes, the GITT measurement was performed, as plotted in (Fig. 4a). The Li^+ diffusion coefficients (D_{Li^+}) are determined using Eq. (1) [18,55]:

$$D_{Li^+} = \frac{4}{\pi\tau}\left(\frac{m_B V_M}{M_B S}\right)^2\left(\frac{\Delta E_S}{\Delta E_\tau}\right)^2 \tag{1}$$

Herein, m_B, V_M, S, and M_B are individually the mass, molar volume, area, and molar mass of electrode, τ is the constant current pulse time, and ΔEs is the difference of two consequent stabilized open circuit potentials. According to the calculation results (Fig. 4b), the $D_{Li}{}^+$ values of Sn/NSPC (in the magnitude of 10^{-8} cm^2/s) are superior to that of the Sn/PC (in the magnitude of 10^{-9} cm^2/s, Fig. S6a) and Sn/NPC (in the range of 10^{-9} to 10^{-8} cm^2/s, Fig. S6b), which means the fast Li^+ diffusion ability in the Sn/NSPC. The larger $D_{Li}{}^+$ for Sn/NSPC is owing to the fact that the N,S co-doping can not solely increase the electronic conductivity of electrode but also supply more defects and active sites on the carbon matrix, which can boost the Li^+ diffusion. In addition, the S atom forms a C-S-C bond with the carbon, which can improve the electrochemical activity of electrode and heighten the storage sites of Li^+, thereby promoting the Li^+ diffusion.

To further understand the high-rate performance of Sn/NSPC electrode, the kinetic analysis was investigated. The CV curves of Sn/NSPC electrode show similar shapes as the scanning rate increases from 0.2 to 1 mV/s (Fig. 4c). In general, the charge-storage mechanism of electrode complies with the following relationship [29,56]:

$$i = av^b \tag{2}$$

Thereinto, a and b are adjustable parameters. To be more specific, b = 0.5 implies a diffusion-controlled process, b = 1.0 means a capacitive process. The b-values are 0.64, 0.81, 0.73 and 0.58, 0.74 (Fig. 4d), separately, indicative of mixed diffusion- and capacitive-controlled processes [57,58]. The capacitive contribution is determined with the subsequent formula [32,59]:

$$i = k_1 v + k_2 v^{1/2} \tag{3}$$

As exhibited in (Fig. 4e), a capacitive contribution of ca. 42.2% of the total charge storage at 0.2 mV/s is acquired for the Sn/NSPC electrode. As the sweep rate increases (Fig. 4f), gradually enhanced capacitive contribution ratios from 42.2% to 64.5% vindicate the capacitive-controlled behavior at high scan rates. In contrast, the CV results of

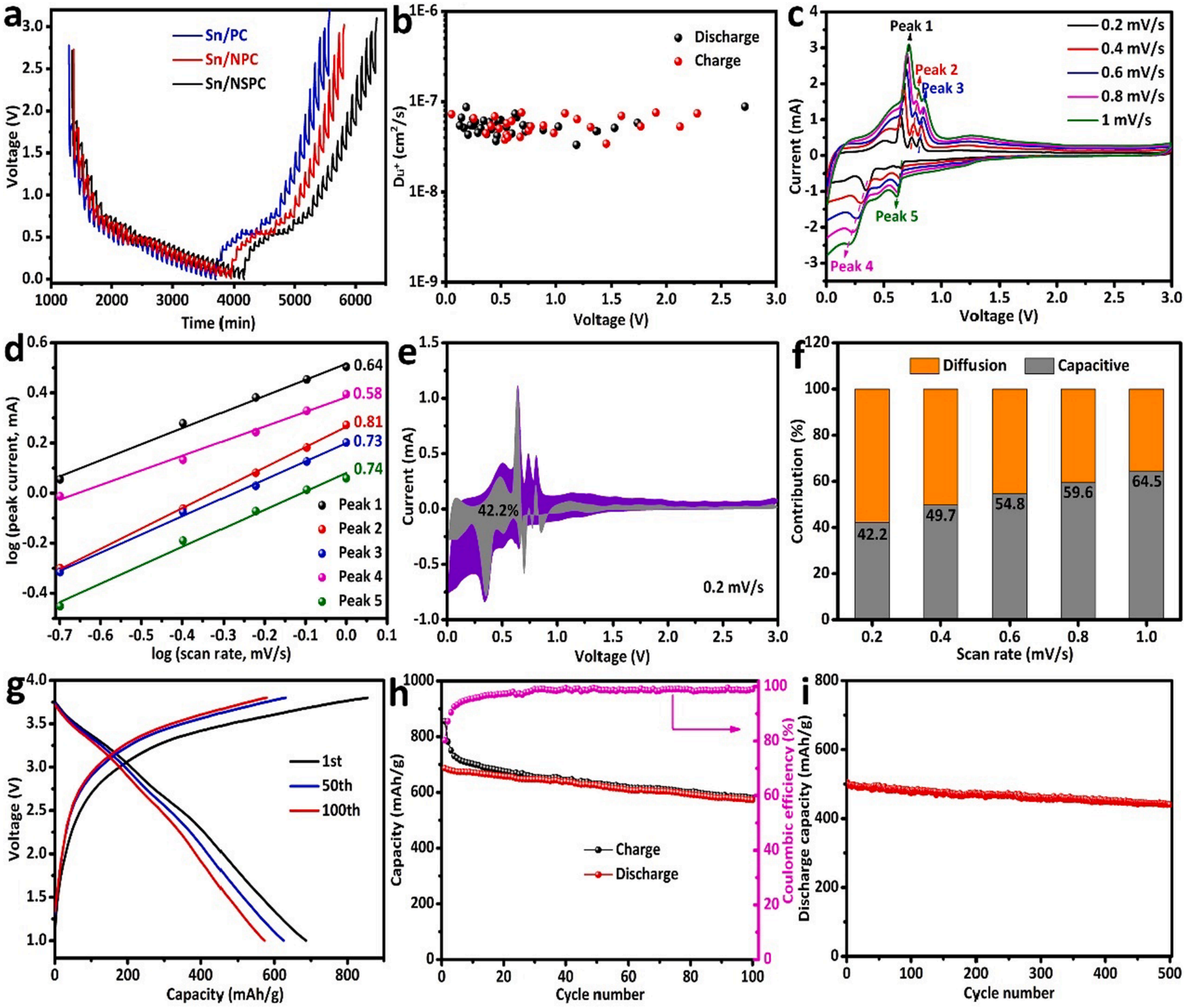

Fig. 4. (a) GITT profiles. (b) The $D_{Li}{}^+$ of Sn/NSPC electrode. (c) CV profiles of Sn/NSPC electrode at various scan rates. (d) b-value determination. (e) Capacitive contribution at 0.2 mV/s. (f) The percentage of capacitive contribution at different scan rates. (g) GCD profiles. Electrochemical performance and the CE of Sn/NSPC||$LiCoO_2$ full cell at (h) 0.1 A/g and (i) 1 A/g.

Sn/PC (Fig. S7) present relatively low capacitive ratios on account of the absence of N, S atoms.

Heartened by the electrochemical performance of half cells, the full cells are assembled by employing the $LiCoO_2$ as cathode to evaluate the potential practicality of Sn/NSPC anode. (Fig. 4g) portrays the CD profiles of the Sn/NSPC||$LiCoO_2$ full cell at 0.1 A/g. The full cell yields an initial charge and discharge capacities of 855.3 and 686.4 mAh/g (according to the anode active material), separately, with an ICE of 80.3%. After 100 cycles, a discharge capacity of 572.6 mAh/g is yielded and CE exceeds 98% (Fig. 4h), revealing the potential practicality in full cells. In addition, after 500 cycles at 1 A/g, the full cell can sustain a discharge capacity of 440.6 mAh/g (Fig. 4i), illustrating the good cycling stability.

DFT calculations were conducted for better understanding the electronic structure of samples. The calculated results indicate a large partial density of states (PDOS) at Fermi level (Fig. 5a, c and e), implying intense metallic characteristic of Sn/PC family. Compared with the Sn/PC (0.26, Fig. 5a) and Sn/NPC (0.36, Fig. 5c), the PDOS around the Fermi level for the Sn/NSPC (Fig. 5e) is 0.42, suggesting that the Sn/NSPC possesses higher electronic conductivity in view of the synergistic effect of N, S co-doping. Specifically, peak values at Fermi level for Sn/PC and Sn/NPC are only 0.26 and 0.36, respectively, while the peak value for Sn/NSPC is 0.42. Better conductivity of one system means better charge transfer at the interface. To understand this, charge density maps at the interface of each system were calculated and rendered (Fig. 5b, d and f). It is clearly shown that the N and S synergistically play a charge channel role at the surface for the Sn/NSPC, while the synergistic effect is only localized in C and N for the Sn/NPC. Therefore, different types of atoms at the interface indicate that synergistic effects are more likely to occur due to the different elements orbital energies overlap, such as S-p, N-p and Sn-d overlap. The S-p orbital electron may be more chance in multi-element system to the energy-similar orbital, rather than in only one single or two element-composed system. In the aspect of theory, this may explain why the Sn/NSPC has the best conductivity among the three systems. Additionally, the electronic conductivity of the sample was further evaluated by four-point probe method. The average electronic conductivities of Sn/PC, Sn/NPC and Sn/NSPC samples are tested to be 2.5×10^{-2}, 4.6×10^{-2} and 6.2×10^{-2} S/cm, separately, which well supports the DFT calculations.

To further figure out the Li^+-storage mechanism of Sn/NSPC electrode, in situ XRD was conducted during the first two CD profiles at 0.15 A/g. From the 2D contour plots of the in situ XRD patterns (Fig. 6a), the peaks at 36.1°, 38.6°, 41.3° and 44.0° are indexed to lithium sheet and BeO (JCPDS NO. 35–0818), which are also observed in (Fig. 6b-c). In the stage I (OCV-0.55 V) of the first lithiation process, the four peak intensities of the Sn progressively decrease, which indicates a continuous

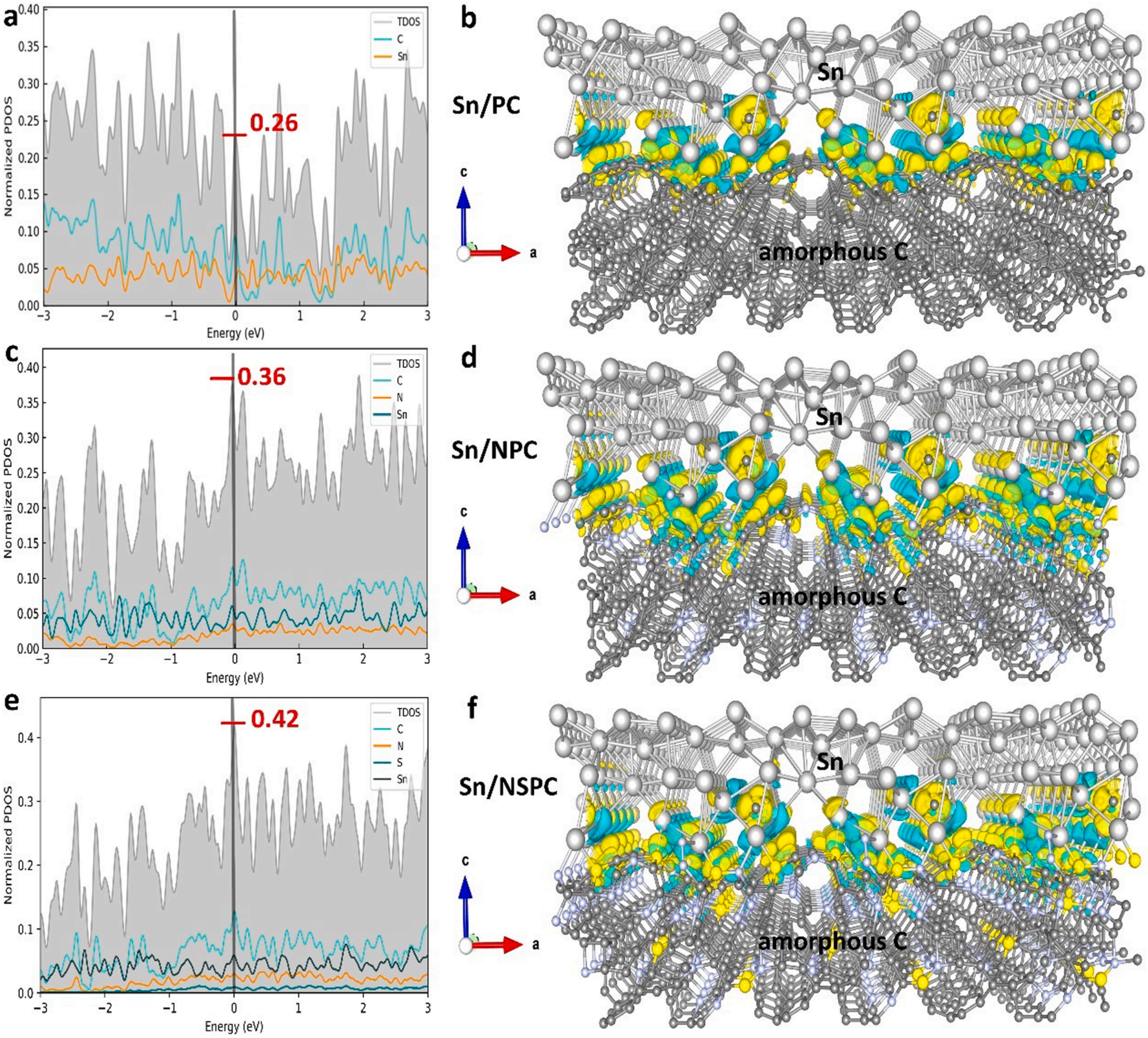

Fig. 5. Partial density of states and charge density difference between amorphous C and Sn of (a-b) Sn/PC, (c-d) Sn/NPC and (e-f) Sn/NSPC. Black, yellow and blue represent C, S and N, respectively. Density map in yellow represents charge accumulation, and the density map in blue represents charge depletion.

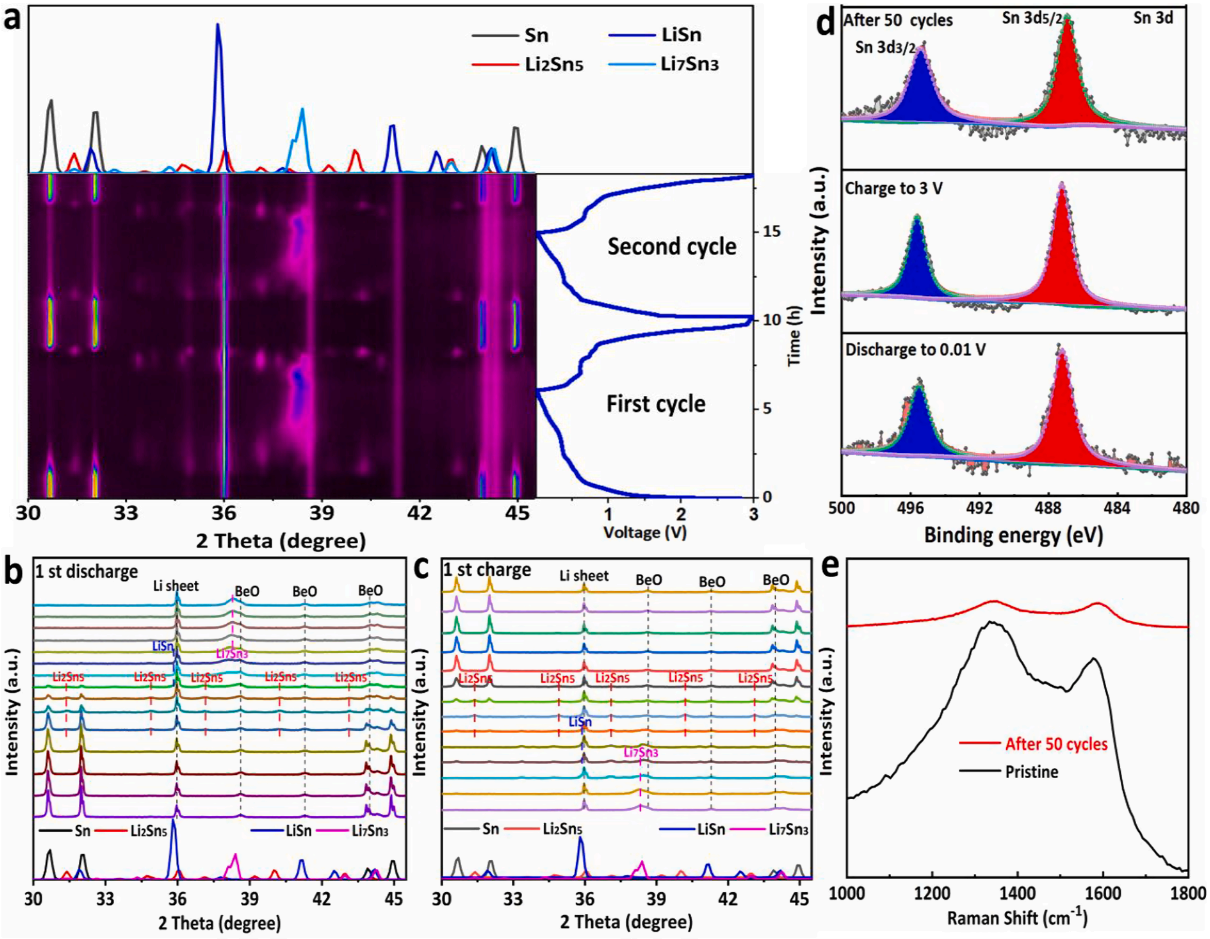

Fig. 6. (a) 2D contour plot of in situ XRD patterns and corresponding voltage curve for the Sn/NSPC electrode during the first two CD process. Selective in situ XRD patterns at various (b) discharge and (c) charge stages. (d) Ex-situ Sn 3d XPS spectra of the Sn/NSPC electrode after 50 cycles, discharged to 0.01 V and charged to 3 V. (e) Raman spectra of the Sn/NSPC electrode before and after 50 cycles.

conversion reaction between the Li^+ and Sn. In the stage II (0.55–0.36 V), the peak intensity from the Sn continues to reduce until the Sn peaks entirely vanish, suggesting the completion of the conversion reaction with Sn transforming into Li_2Sn_5 (31.4°, 34.9°, 37.1°, 40.2° and 43.1°). In the stage III (0.36–0.26 V), these peaks from the Li_2Sn_5 gradually lower in intensity and disappear. Meanwhile, a new peak at about 35.9° gradually appears, corresponding to the formation of LiSn. The occurrence of LiSn is stemmed from the alloying reaction between Li_2Sn_5 and Li^+. In the stage IV (0.26–0.15 V), the peaks of LiSn gradually lower until it vanishes thoroughly, followed by the emergence of a new peak situated at 38.3° (stage V, from 0.15 to 0.01 V). The new peak at 38.3° is assigned to Li_7Sn_3. Therefore, the Li^+-storage mechanisms of Sn/NSPC electrode can be concluded as "Sn → Li_2Sn_5 → LiSn → Li_7Sn_3" during the discharge process. The variations in the subsequent charging process are inverse to the discharging process. The de-alloying/alloying reaction in the next cycle is similar to that in the initial cycle.

The ex-situ XPS spectra were collected at various CD states and cycle number for the Sn/NSPC electrode (initial discharge to 0.01 V, charge to 3 V and after 50 cycles). As exhibited in (Fig. 6d), two obvious peaks of Sn $3d_{5/2}$ (487.2 eV) and Sn $3d_{3/2}$ (495.6 eV) are in accord with that of fresh Sn/NSPC electrode (Fig. 2f), indicating the structural stability of Sn/NSPC during the electrochemical process. The XRD pattern of Sn/NSPC electrode after 200 cycles demonstrates its structural stability again (Fig. S8). Furthermore, the Raman spectra of Sn/NSPC before and after 50 cycles are displayed in (Fig. 6e). As the number of cycles raises to 50, the line width of D-band adds as well, which suggests that amorphous C becomes less ordered and possesses defects [48]. These defect sites offer more electrochemically active locations, thereby improving electrode specific capacity [48,60].

4. Conclusions

To sum up, we have successfully fabricated N, S co-doped porous carbon/Sn composites with synergistic effect via a simple self-derived templating strategy, in which Na_2CO_3 generated by carbonization of mixture of DSSC and thiourea is served as a sacrificial template. The N, S co-doped porous carbon cannot only offer additional space to buffer the volume variation but also introduce more defects in the C matrix for the Li storage. More importantly, the DFT calculations confirm the synergistic effect of N, S co-doping, which can effectively heighten the electronic conductivity. In addition, in-situ XRD reveals the detailed lithium storage mechanisms. Worked as an anode in LIBs, the Sn/NSPC renders the best lithium-storage properties among the three electrodes. Besides, the full cell assembled reaches a discharge capacity of 572.6 mAh/g after 100 cycles and good cycling stability up to 440.6 mAh/g after 500 cycles. In general, the Sn/NSPC composite possesses enormous potential as a new anode material for the next generation high capacity LIBs. Furthermore, this strategy herein has the advantages of decreasing the synthesis cost and simplifying the synthetic routes that possesses a great prospect for realistic application.

CRediT authorship contribution statement

Kun Liu: Conceptualization, Methodology, Writing – original draft.

Hongfei Zheng: Formal analysis, Data curation. **Jia-ao Wang:** Methodology, Software, Visualization. **Yuhao Zhou:** Data curation. **Ning Zhang:** Data curation. **Yehong Du:** Data curation. **Jianzong Man:** Methodology. **Graeme Henkelman:** Supervision. **Juncai Sun:** Supervision, Writing – review & editing, Funding acquisition.

Declaration of Competing Interest

The authors declare that they have no known competing financial interests or personal relationships that could have appeared to influence the work reported in this paper.

Acknowledgements

This work was supported by the Foundation Research Funds for the Central University (No. 3132019328) in China. Calculations at UT Austin were supported by the Welch Foundation (F-1841) and the Texas Advanced Computing Center in the United States. The authors thank Siyuan Wang from Shiyanjia Lab (www.shiyanjia.com) for the support of TEM, EA and XPS tests.

Appendix A. Supplementary material

Supplementary data to this article can be found online at https://doi.org/10.1016/j.apsusc.2021.152319.

References

[1] J. Zhu, W. Tu, H. Pan, H. Zhang, B. Liu, Y. Cheng, Z. Deng, H. Zhang, Self-Templating Synthesis of Hollow Co_3O_4 Nanoparticles Embedded in N, S-Dual-Doped Reduced Graphene Oxide for Lithium Ion Batteries, ACS Nano 14 (2020) 5780–5787.

[2] M. Guo, W. Meng, X. Zhang, X. Liu, Z. Bai, S. Chen, Z. Wang, F. Yang, Electrochemical behavior and self-organization of porous Sn nanocrystals@ acetylene black microspheres in lithium-ion half cells, Appl. Surf. Sci. 470 (2019) 36–43.

[3] X. Chen, S. Zeng, H. Muheiyati, Y. Zhai, C. Li, X. Ding, L. Wang, D. Wang, L. Xu, Y. He, Y. Qian, Double-shelled Ni-Fe-P/N-doped carbon nanobox derived from Prussian blue analogue as electrode material for K-ion batteries and Li-S batteries, ACS Energy Lett. 4 (2019) 1496–1504.

[4] R. Li, S. Nie, C. Miao, Y. Xin, H. Mou, G. Xu, W. Xiao, Heterostructural Sn/SnO_2 microcube powders coated by a nitrogen-doped carbon layer as good-performance anode materials for lithium ion batteries, J. Colloid Interf. Sci. 606 (2022) 1042–1054.

[5] M. Bai, X. Tang, C. Sun, Y. Zhang, W. Wu, S. Li, S. Liu, W. Zhao, Y. Ma, Ternary Anode Design for Sustainable Battery Technology: An Off-Stoichiometric Sn/ $SnSiO_{x+2}$@C Composite Recycled from Biomass, ACS Sustainable Chem. Eng. 7 (2019) 12563–12573.

[6] H. Tian, Y. Liang, J. Repac, S. Zhang, C. Luo, S.-C. Liou, G. Wang, S.H. Ehrman, W.-Q. Han, Rational Design of Core-Shell-Structured Particles by a One-Step and Template-Free Process for High-Performance Lithium/Sodium Ion Batteries, J. Phys. Chem. C 122 (2018) 22232–22240.

[7] P. Sun, J. Davis, L. Cao, Z. Jiang, J.B. Cook, H. Ning, J. Liu, S. Kim, F. Fan, R. G. Nuzzo, P.V. Braun, High capacity 3D structured tin-based electroplated Li-ion battery anodes, Energy Storage Mater. 17 (2019) 151–156.

[8] M. Yang, L. Liu, H. Yan, W. Zhang, D. Su, J. Wen, W. Liu, Y. Yuan, J. Liu, X. Wang, Porous nitrogen-doped Sn/C film as free-standing anodes for lithium ion batteries, Appl. Surf. Sci. 551 (2021), 149246.

[9] Y. Liu, J. Sun, H. Du, S. He, L. Xie, W. Ai, W. Huang, A long-cycling anode based on a coral-like Sn nanostructure with a binary binder, Chem. Commun. 55 (2019) 10460–10463.

[10] K.J. Rhodes, R. Meisner, M. Kirkham, N. Dudney, C. Daniel, In Situ XRD of Thin Film Tin Electrodes for Lithium Ion Batteries, J. Electrochem. Soc. 159 (3) (2012) A294–A299.

[11] B.T. Heligman, K.J. Kreder, A. Manthiram, Zn-Sn Interdigitated Eutectic Alloy Anodes with High Volumetric Capacity for Lithium-Ion Batteries, Joule 3 (4) (2019) 1051–1063.

[12] H. Zhang, T. Shi, D.J. Wetzel, R.G. Nuzzo, P.V. Braun, 3D Scaffolded Nickel-Tin Li-Ion Anodes with Enhanced Cyclability, Adv. Mater. 28 (4) (2016) 742–747.

[13] J. Ryu, H. Kim, J. Kang, H. Bark, S. Park, H. Lee, Dual Buffering Inverse Design of Three-Dimensional Graphene-Supported Sn-TiO_2 Anodes for Durable Lithium-Ion Batteries, Small 16 (46) (2020) 2004861, https://doi.org/10.1002/smll.v16.4610.1002/smll.202004861.

[14] L. Sun, X. Wang, R.A. Susantyoko, Q. Zhang, High performance binder-free Sn coated carbon nanotube array anode, Carbon 82 (2015) 282–287.

[15] X. Huang, S. Cui, J. Chang, P.B. Hallac, C.R. Fell, Y. Luo, B. Metz, J. Jiang, P. T. Hurley, J. Chen, A hierarchical tin/carbon composite as an anode for lithium-ion batteries with a long cycle life, Angew. Chem. Int. Ed. 54 (5) (2015) 1490–1493.

[16] Y. Cheng, Z. Yi, C. Wang, Y. Wu, L. Wang, Controllable fabrication of C/Sn and C/SnO/Sn composites as anode materials for high-performance lithium-ion batteries, Chem. Eng. J. 330 (2017) 1035–1043.

[17] H.-G. Wang, C. Yuan, R. Zhou, Q. Duan, Y. Li, Self-sacrifice template formation of nitrogen-doped porous carbon microtubes towards high performance anode materials in lithium ion batteries, Chem. Eng. J. 316 (2017) 1004–1010.

[18] W. Gou, X. Kong, Y. Wang, Y. Ai, S. Liang, A. Pan, G. Cao, Yolk-shell structured V_2O_3 microspheres wrapped in N, S co-doped carbon as pea-pod nanofibers for high-capacity lithium ion batteries, Chem. Eng. J. 374 (2019) 545–553.

[19] Q. Wang, J. Yang, X. Zhou, J. Tang, H. Zhong, M. Jia, M. Cui, M. Jiang, H. Wang, N, S Co-Doped Hierarchical Porous Carbon from Antibiotic Bacteria Residues as Anode Materials for Lithium Ion Batteries, J. Electrochem. Soc. 166 (4) (2019) A704–A710.

[20] D. Li, X. Ren, Q. Ai, Q. Sun, L. Zhu, Y. Liu, Z. Liang, R. Peng, P. Si, J. Lou, J. Feng, L. Ci, Facile Fabrication of Nitrogen-Doped Porous Carbon as Superior Anode Material for Potassium-Ion Batteries, Adv. Energy Mater. 8 (2018) 1802386–1802394.

[21] Y. Zeng, Y. Huang, N. Liu, X. Wang, Y. Zhang, Y. Guo, H.-H. Wu, H. Chen, X. Tang, Q. Zhang, N-doped porous carbon nanofibers sheathed pumpkin-like Si/C composites as free-standing anodes for lithium-ion batteries, J. Energy Chem. 54 (2021) 727–735.

[22] J. Xu, D. Su, W. Zhang, W. Bao, G. Wang, Nitrogen-Sulfur Co-doped Porous Graphene Matrix as a Sulfur Immobilizer for High Performance Lithium Sulfur Battery, J. Mater. Chem. A 4 (2016) 17381–17393.

[23] Q. Hu, Y. Meng, H. Zhang, G. Zhao, J. Hu, F. Zhu, Y. Zhang, Encapsulated Ni_3S_2 nanoparticles with N, S dual-doped carbon nanotubes: A robust structure for lithium storage, J. Electroanal. Chem. 873 (2020) 114383–114390.

[24] H. Su, Y. Zhang, X. Liu, F. Fu, J. Ma, K. Li, W. Zhang, J. Zhang, D. Li, Construction of CoP@C embedded into N/S-co-doped porous carbon sheets for superior lithium and sodium storage, J. Colloid Interf. Sci. 582 (2021) 969–976.

[25] J. Wang, K. Jiang, B. Shen, M. Zhen, Synergetic Effect of Nitrogen/Sulfur Dual-Doped Hierarchically Porous Carbon Networks for Li−S Batteries, ACS Sustainable Chem. Eng. 8 (2) (2020) 749–758.

[26] S. Wu, D. Wei, Y. Yin, Q. Li, H. Wang, W. Chen, Y. Jiang, X. Tao, N, S co-doped activated carbon with porous architecture derived from partial poly (2, 2’-dithiodianiline) for supercapacitors, J. Energy Chem. 33 (2021) 102043–102052.

[27] B.o. Yin, X. Cao, A. Pan, Z. Luo, S. Dinesh, J. Lin, Y. Tang, S. Liang, G. Cao, Encapsulation of CoS_x Nanocrystals into N/S Co-Doped Honeycomb-Like 3D Porous Carbon for High-Performance Lithium Storage, Adv. Sci. 5 (9) (2018) 1800829, https://doi.org/10.1002/advs.201800829.

[28] K. Liu, J.-A. Wang, H. Zheng, X. Sun, Z. Yang, J. Man, X. Wang, J. Sun, Direct synthesis of tin spheres/nitrogen-doped porous carbon composite by self-formed template method for enhanced lithium storage, J. Mater. Sci. Technol. 104 (2022) 88–97.

[29] F. Zeng, M. Yu, W. Cheng, W. He, Y. Pan, Y. Qu, C. Yuan, Tunable Surface Selenization on MoO_2-Based Carbon Substrate for Notably Enhanced Sodium-Ion Storage Properties, Small 16 (41) (2020) 2001905, https://doi.org/10.1002/smll.v16.4110.1002/smll.202001905.

[30] H.J. Monkhorst, J.D. Pack, Special points for Brillouin-zone integrations, Phys. Rev. B 13 (1976) 5188–5192.

[31] Y. Wang, X. Zhao, Z.-H. Liu, Few-layer WS_2 nanosheets with oxygen-incorporated defect-sulphur entrapped by a hierarchical N, S co-doped graphene network towards advanced long-term lithium storage performances, RSC Adv. 10 (12) (2020) 7134–7145.

[32] W.Q. Yao, S.B. Wu, L. Zhan, Y.L. Wang, Two-dimensional porous carbon-coated sandwich-like mesoporous SnO_2/graphene/mesoporous SnO_2 nanosheets towards high-rate and long cycle life lithium-ion batteries, Chem. Eng. J. 361 (2019) 329–341.

[33] K. Wu, Y. Feng, J. Huang, C. Bai, M. He, Mo-doped 3D carbon@Sn as high performance anode material for lithium ion batteries, Chem. Phys. Lett. 756 (2020) 137832–137839.

[34] L. Zhang, J. Liu, W. Wang, D. Li, C. Wang, P. Wang, K. Zhu, Z. Li, Synthesis of N-doped multi-cavity Sn/C composite and utilization to anode in lithium ion batteries, Mater. Chem. Phys. 260 (2021) 124199–124207.

[35] F. Zhang, Y. Wang, W. Guo, S. Rao, P. Mao, Synthesis of Sn-MnO@nitrogen-doped carbon yolk-shelled three-dimensional interconnected networks as a high-performance anode material for lithium-ion batteries, Chem. Eng. J. 360 (2019) 1509–1516.

[36] Y. Liu, N. Zhang, L. Jiao, J. Chen, Tin Nanodots Encapsulated in Porous Nitrogen-Doped Carbon Nanofibers as a Free-Standing Anode for Advanced Sodium-Ion Batteries, Adv. Mater. 27 (42) (2015) 6702–6707.

[37] X.u. Gao, B. Wang, Y. Zhang, H. Liu, H. Liu, H. Wu, S. Dou, Graphene-scroll-sheathed α-MnS coaxial nanocables embedded in N, S Co-doped graphene foam as 3D hierarchically ordered electrodes for enhanced lithium storage, Energy Storage Mater. 16 (2019) 46–55.

[38] J. Cui, Y. Qiu, H. Zhang, Z. Yao, W. Zhao, Y. Liu, J. Sun, Sulfur- and nitrogen-doped rice husk-derived C/SiO_x composites as high-performance lithium-ion battery anodes, Solid State Ionics 361 (2021) 115548–115556.

[39] J. Zhu, Z. Zhang, X. Ding, J.-P. Cao, G. Hu, In situ one–pot synthesis of Sn/ lignite–based porous carbon composite for enhanced lithium storage, J. Colloid Interface Sci. 587 (2021) 367–375.

[40] F. Zhang, Y. Wang, W. Guo, P. Mao, S. Rao, P. Xiao, Yolk-shelled Sn@C@MnO hierarchical hybrid nanospheres for high performance lithium-ion batteries, J. Alloy. Compd. 829 (2020) 154579–154587.

[41] D. Li, L. Chen, L. Chen, Q. Sun, M. Zhu, Y. Zhang, Y. Liu, Z. Liang, P. Si, J. Lou, J. Feng, L. Ci, Potassium gluconate-derived N/S Co-doped carbon nanosheets as superior electrode materials for supercapacitors and sodium-ion batteries, J. Power Sources 414 (2019) 308–316.

[42] C. Yang, J. Ren, M. Zheng, M. Zhang, Z. Zhong, R. Liu, J. Huang, J. Lan, Y. Yu, X. Yang, High-level N/P co-doped Sn-carbon nanofibers with ultrahigh pseudocapacitance for high-energy lithium-ion and sodium-ion capacitors, Electrochim. Acta 359 (2020) 136898–136908.

[43] D. Guo, Z. Zhang, B. Xi, Z. Yu, Z. Zhou, X. Chen, Ni_3S_2 anchored into N/S co-doped reduced graphene oxide with highly pleated structure as a sulfur host for lithium-sulfur batteries, J. Mater. Chem. A 8 (2020) 3834–3844.

[44] L. Sun, T. Ma, J. Zhang, X. Guo, C. Yan, X. Liu, Double-shelled hollow carbon spheres confining tin as high-performance electrodes for lithium ion batteries, Electrochim. Acta 321 (2019) 134672–134679.

[45] K. Wang, K. Zhao, Y. Wang, H. Li, H. Jiang, L. Chen, N, S co-doped carbon confined MnO/MnS heterostructures derived from a one-step pyrolysis of Mn-methionine frameworks for advanced lithium storage, J. Alloy. Compd. 860 (2020) 158451–158458.

[46] X. Yang, Z. Ran, F. Luo, Y. Li, P. Zhang, H. Mi, Free-standing ZIF-8 derived nitrogen and sulfur co-doped porous carbon nanofibers host for high mass loading lithium-sulfur battery, Appl. Surf. Sci. 509 (2020) 145270–145277.

[47] S. Ding, W. Cheng, L. Zhang, G. Du, X. Hao, G. Nie, B. Xu, M. Zhang, Q. Su, C. A. Serra, Organic molecule confinement reaction for preparation of the Sn nanoparticles@graphene anode materials in Lithium-ion battery, J. Colloid Interface Sci. 589 (2021) 308–317.

[48] X. Li, Y.u. Zhong, M. Cai, M.P. Balogh, D. Wang, Y. Zhang, R. Li, X. Sun, Tin-alloy heterostructures encapsulated in amorphous carbon nanotubes as hybrid anodes in rechargeable lithium ion batteries, Electrochim. Acta 89 (2013) 387–393.

[49] J.H. Lee, S.H. Oh, S.Y. Jeong, Y.C. Kang, J.S. Cho, Rattle-type porous Sn/C composite fibers with uniformly distributed nanovoids containing metallic Sn nanoparticles for high-performance anode materials in lithium-ion batteries, Nanoscale 10 (45) (2018) 21483–21491.

[50] C.D. Gu, Y.J. Mai, J.P. Zhou, Y.H. You, J.P. Tu, Non-aqueous electrodeposition of porous tin-based film as an anode for lithium-ion battery, J. Power Sources 214 (2012) 200–207.

[51] J. Zeng, C. Peng, R. Wang, C. Cao, X. Wang, J. Liu, Magnetic Sn/SnO/$FeSn_2$ nanocomposite as a high-performance anode material for lithium-ion batteries, Powder Technol. 364 (2020) 719–724.

[52] K. Xu, X. Shen, Z. Yan, Z. Ji, A. Yuan, G. Zhu, L. Kong, J. Zhu, B. Li, Cyanometallic framework-derived dual-buffer structure of Sn-Co based nanocomposites for high-performance lithium storage, J. Alloy. Compd. 830 (2020) 154680–154688.

[53] Y. Lou, H. Di, C. Li, C. Liang, Y. Yu, Z. Shi, D. Zhang, X.-B. Chen, S. Feng, Delicately designed Sn-based electrode material via spray pyrolysis for high performance lithium-ion battery, Electrochim. Acta 318 (2019) 542–550.

[54] Y. Liu, Y. Qiao, G.Y. Wei, S. Li, Z.S. Lu, X.B. Wang, X.D. Lou, Sodium storage mechanism of N, S co-doped nanoporous carbon: Experimental design and theoretical evaluation, Energy Storage Mater. 11 (2018) 274–281.

[55] G. Liu, M. Huang, Z. Zhang, B. Xi, H. Li, S. Xiong, Robust S-doped TiO_2@N, S-codoped carbon nanotube arrays as free-binder anodes for efficient sodium storage, J. Energy Chem. 53 (2021) 175–184.

[56] J. Cai, R. Cai, Z. Sun, X. Wang, N. Wei, F. Xu, Y. Shao, P. Gao, S. Dou, J. Sun, Confining TiO_2 Nanotubes in PECVD-Enabled Graphene Capsules Toward Ultrafast K-Ion Storage, In Situ TEM/XRD Study and DFT Analysis, Nano-Micro Lett. 12 (2020) 123.

[57] S.-B. Xia, L.-F. Yao, H. Guo, X. Shen, J.-M. Liu, F.-X. Cheng, J.-J. Liu, Li^+ intercalcation pseudocapacitance in Sn-based metal-organic framework for high capacity and ultra-stable Li ion storage, J. Power Sources 440 (2019) 227162–227170.

[58] C. Chen, Y. Wen, X. Hu, X. Ji, M. Yan, L. Mai, P. Hu, B. Shan, Y.H. Huang, Na^+ intercalation pseudocapacitance in graphene-coupled titanium oxide enabling ultra-fast sodium storage and long-term cycling, Nat. Commun. 6 (2015) 6929.

[59] N. Shi, Y. Chu, B. Xi, M. Huang, W. Chen, B. Duan, C. Zhang, J. Feng, S. Xiong, Sandwich Structures Constructed by ZnSe⊂N-C@$MoSe_2$ Located in Graphene for Efficient Sodium Storage, Adv. Energy Mater. 10 (41) (2020) 2002298, https://doi.org/10.1002/aenm.v10.4110.1002/aenm.202002298.

[60] X. Li, J. Liu, Y. Zhang, Y. Li, H. Liu, X. Meng, J. Yang, D. Geng, D. Wang, R. Li, X. Sun, High concentration nitrogen doped carbon nanotube anodes with superior Li^+ storage performance for lithium rechargeable battery application, J. Power Sources 197 (2012) 238–245.